Palaeogeography, Palaeoclimatology, Palaeoecology 421 (2015) 48–59

Contents lists available at ScienceDirect

Palaeogeography, Palaeoclimatology, Palaeoecology

journal homepage: www.elsevier.com/locate/palaeo

Late Miocene stepwise aridification in the Asian interior and the interplay between tectonics and climate

Jimin Sun [a,b,*], Zhijun Gong [a], Zhonghua Tian [a], Yingying Jia [a], Brian Windley [c]

[a] Key Laboratory of Cenozoic Geology and Environment, Institute of Geology and Geophysics, Chinese Academy of Sciences, P.O. Box 9825, Beijing 100029, China
[b] CAS Center for Excellence in Tibetan Plateau Earth Sciences
[c] Department of Geology, The University of Leicester, Leicester LE1 7RH, UK

ARTICLE INFO

Article history:
Received 6 September 2014
Received in revised form 22 December 2014
Accepted 7 January 2015
Available online 10 January 2015

Keywords:
Late Cenozoic
Aridification
Paleoclimate
Forcing mechanism
Central Asia

ABSTRACT

The mid-latitudinal central Asian continent is characterized by large sand deserts and Gobi (stony desert). In this context, it is of interest to study the timing and forcing mechanisms of aridification in the region. Here we present multiple geochemical climatic proxies from late Cenozoic strata in the Tarim Basin of northwestern China, a region sensitive to climatic change. The results yield long-term climatic records covering a time interval of 13.3 to 2.5 Ma. We find that a general trend towards a dry climate was superimposed by two stepwise aridification events, the first lesser aridity phase occurred at ~7–5.3 Ma and the second extreme aridity episode was initiated at ~5.3 Ma. Based on the correlation between climatic change and regional tectonic events, we propose a mechanism to explain the climatic variations. The general long-term drying trend since the mid-Miocene was a response to global climatic cooling, while the stepwise aridification since the latest Miocene was controlled mainly by regional tectonic uplift.

1. Introduction

The mid-latitude Asian interior is characterized by several large deserts (e.g., Kara Kum, Kyzyl Kum, Taklimakan, Junggar) between 30°N and 50°N, constituting the largest mid-latitude arid zone in the Northern Hemisphere. At present, a dry climate prevails in these regions due to their location far from oceans and/or the rain-shadow effect of High Asia (Zhu et al., 1980). Considering the vastness of the dry areas, it is important to understand the history of the aridity and the associated forcing mechanisms of aridification in the region.

Although the onset of aridity in the Asian interior has been studied in recent decades, there is no consensus regarding its timing (e.g., Dupont-Nivet et al., 2007; Sun et al., 2010; Xiao et al., 2010; Tang et al., 2011; Hoorn et al., 2012; Dong et al., 2013). Compared with studies on the Paleogene arid environment in the Tarim Basin (e.g., Bosboom et al., 2013, 2014), more studies have focused on the enhanced aridification after the Miocene, especially for the formation of the Taklimakan Desert within the Tarim Basin (e.g., Fang et al., 2002; Zheng et al., 2002, 2003, 2010a,b; Sun and Liu, 2006; Sun et al., 2008, 2009b, 2011; Tada et al., 2010; Chang et al., 2012; Liu et al., 2014; Wang et al., 2014). However, the timing of the formation of the Taklimakan desert is not well constrained; for example, Fang et al. (2002) reported a formation age of mid-Pleistocene, whereas others suggested the latest Miocene (e.g., Sun and Liu, 2006; Sun et al., 2009b; Chang et al., 2012; Liu et al., 2014).

Similar to the timing of the aridity, there is also debate about the forcing mechanisms of the aridification event. The results of general circulation modeling indicate that the uplift of the Tibetan Plateau, caused by India–Asia collision, directly drove the stepwise aridification of the Asian interior during the late Cenozoic (Manabe and Terpstra, 1974; Kutzbach et al., 1989; Ruddiman and Kutzbach, 1989; Manabe and Broccoli, 1990; Raymo and Ruddiman, 1992; Liu et al., 2003). More recent studies suggest that the retreat of the Paratethys Sea was responsible for the aridification in the Asian interior (e.g., Ramstein et al., 1997; Zhang et al., 2007; Bosboom et al., 2013) or that global factors (i.e., global cooling) rather than regional factors drove the late Cenozoic aridification (e.g., Lu et al., 2010; Miao et al., 2011, 2012, 2013).

Among the large inland basins in central Asia, the Tarim Basin is most known for its size (~530,000 km^2) and active sand dunes. This basin is constrained by three of Asia's large mountain ranges: the Tian Shan to the north, the Pamir Mountains to the west, and the Kunlun range to the south (Fig. 1). Located in the rain-shadow of the Tibetan Plateau, the climate in the basin is extremely dry with annual rainfall of less than 50 mm in the center of the basin, making it the driest region in the interior of Asia. On account of the chronology and relative continuity of late Cenozoic sediments (Sun et al., 2009a), we focused on studying the paleoclimatic changes recorded in the northern Tarim Basin.

This paper has two main objectives: (1) to construct multiple high-resolution geochemical climatic records during the late Cenozoic; and

* Corresponding author. Tel.: + 86 10 8299 8389; fax: + 86 10 6201 0846.
E-mail address: jmsun@mail.igcas.ac.cn (J. Sun).

http://dx.doi.org/10.1016/j.palaeo.2015.01.001
0031-0182/

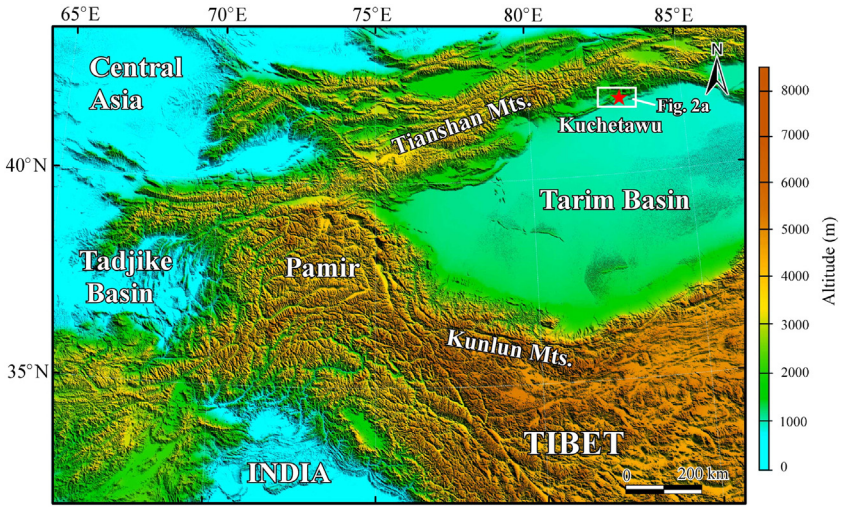

Fig. 1. Digital elevation model of the Tarim Basin and surrounding region, together with the location of the study section.

(2) to explain the history of aridity in the region and to discuss the interplay between tectonics and climate.

2. Geological setting

The study region is the foreland basin of the southern Tian Shan (Fig. 1), where Cenozoic deposits have been tectonically deformed, forming a series of anticlines and synclines as a result of Cenozoic north–south crustal shortening in response to intracontinental deformation related to the India–Eurasia convergence. These anticlines are associated with the propagation of thrust faults as a consequence of southward thrusting of the southern Tian Shan (e.g., Windley et al., 1990; Deng et al., 2000; Fu et al., 2003, 2010; Hubert-Ferrari et al., 2007). The present study focuses on the Qiulitag anticline, which is an east–west trending mountainous ridge that extends for 340 km and has a width of 5–7 km (Fig. 2a).

The Kuchetawu section, forming the focus of this study, is located in the eastern part of the Qiulitag anticline (41°55.097′N, 83°03.280′E), exposed by the southward flowing Kuqa River (Fig. 2a). Field investigations indicate that the section is a sub-vertical anticlinal isocline

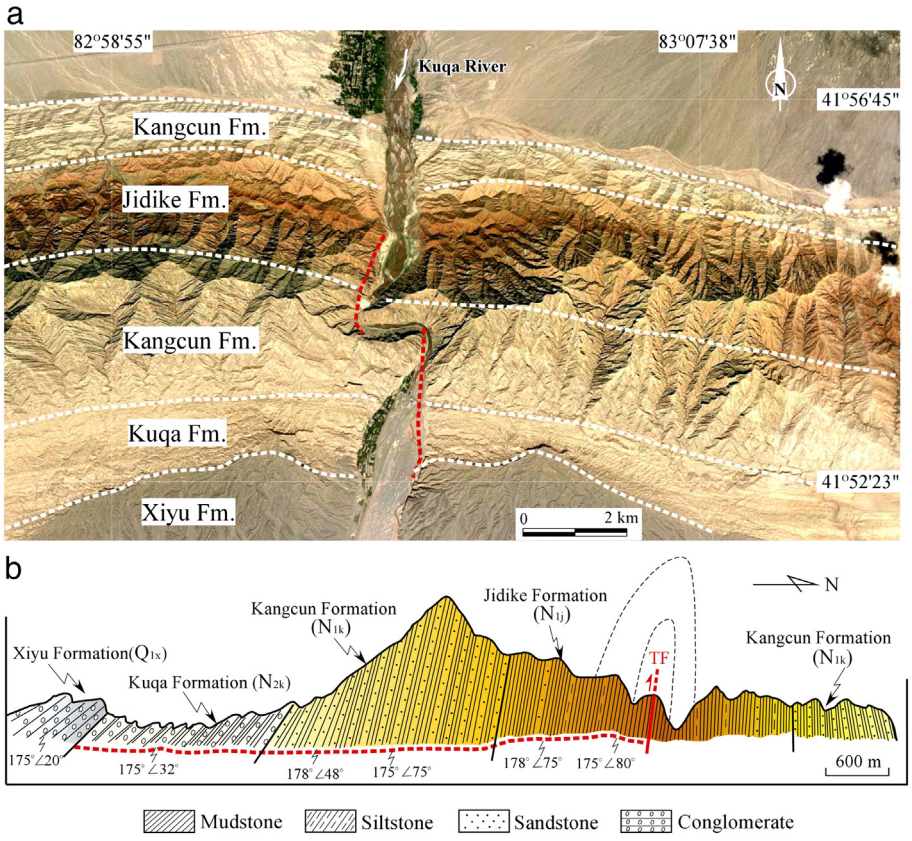

Fig. 2. The Qiulitag anticline and cross-section sketch at Kuchetawu. a, The Qiulitag anticline in the foreland basin of the southern Tian Shan range; b, exposed Cenozoic strata of the Kuchetawu section. The bold dashed line shows the sampling route. N_{1j}: middle Miocene Jidike Formation; N_{1k}: late Miocene Kangcun Formation; N_{2k}: Pliocene Kuqa Formation; Q_{1x}: early Pleistocene Xiyu Formation; TF: Thrust Fault.

overturned to the north (Fig. 2b). The southern limb is well exposed with an almost continuous section including the middle Miocene Jidike Formation, the late Miocene Kangcun Formation, the Pliocene Kuqa Formation and the Lower Pleistocene Xiyu Formation. Its northern limb has been eroded and only contains the relict Kangcun Formation (Fig. 2a, b); hence, our sampling focused on the southern limb. Generally, there is a trend towards coarser particle size and lighter color when moving from the core to the limbs of the anticline (Fig. 2b).

3. Sedimentary facies and ages

The sedimentary facies of the Kuchetawu section are diverse (Fig. 3). The oldest stratum is the middle Miocene Jidike Formation (N_{1j}), which is dominated by reddish mudstones with occasional intercalations of gray sandstone or siltstone, with a total thickness of 1170 m. Horizontal laminations are very common, and the thickness of the laminations is usually less than 2 cm; such sedimentary features together with the general fine particle size imply a predominantly lacustrine environment. Although there are occasional very thin (less than 2 cm thick) interbedded gypsum layers, it is not sure if they are primary chemical deposits in saline lakes or secondary minerals formed after initial deposition of the sediments due to sedimentary structures (e.g., bedding plane, water-escape structures). The late Miocene Kangcun Formation (N_{1k}) consists of interbedded gray sandstones and reddish to brownish mudstones with a total thickness of 1770 m. Generally most sandstone beds are 30 to 100 cm or >100 cm thick, whereas the interbedded mudstones usually with horizontal bedding; such sedimentary features mostly represent fluvial–lacustrine deposition in a foreland basin. The Pliocene Kuqa Formation (N_{2k}) can be subdivided into two parts: the lower is composed of interbedded gray conglomerates and brownish mudstone or siltstone, while the upper is dominated by gray conglomerates with thin intercalated brownish siltstone layers. The total thickness of the Kuqa Formation is 840 m. The conglomerates reach a maximum thickness of 8–10 m thick, and the largest gravel sizes can be up to 10 cm; such coarse deposits were transported by high-energy floods from the nearby Tian Shan orogen. The horizontal beddings of the intercalated fine-grained mudstone or siltstone mostly represent lake environments. Therefore, the sedimentary facies can be interpreted as a high-energy fluvial or alluvial source interfinger with ephemeral lacustrine sediments. The early Pleistocene Xiyu Formation (Q_{1x}) consists mainly of pebble to boulder conglomerates, implying high-energy alluvial fan deposition in a foreland basin. It has a thickness in excess of 1000 m.

The ages of the Kuchetawu section are based on both biostratigraphic age control and high-resolution magnetostratigraphy. A fossil tooth of *Hipparion chiai* was discovered at a thickness of 3100 m (from top to bottom) in the section (Fig. 4a), corresponding to the Vallesian Age of the European Neogene mammal zones (MN) 9/10 (Deng, 2006), with an age range of 11–9 Ma and centered at about 10 Ma. Based on the above biostratigraphic age constraints, the measured magnetic polarity sequence was correlated with the geomagnetic polarity timescale (GPTS) of Cande and Kent (1995), and yielded an age range of 13.3 to 2.6 Ma (Sun et al., 2009a) (Fig. 4a). The relationship between the thickness of the study section and the age of the sediments (based on the magnetostratigraphic correlations) was used to yield the age chronology used in this study (Fig. 4b).

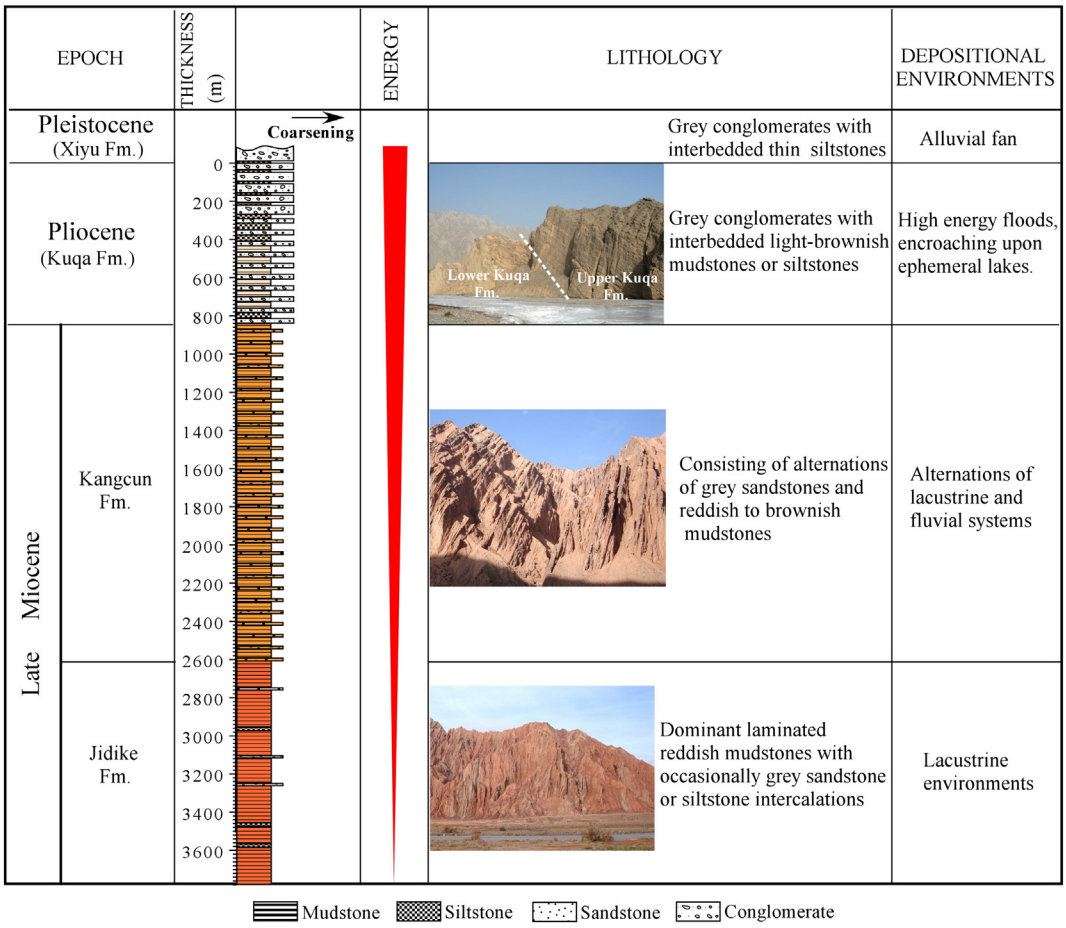

Fig. 3. Lithology and sedimentary facies of the Kuchetawu section in the northern Tarim Basin.

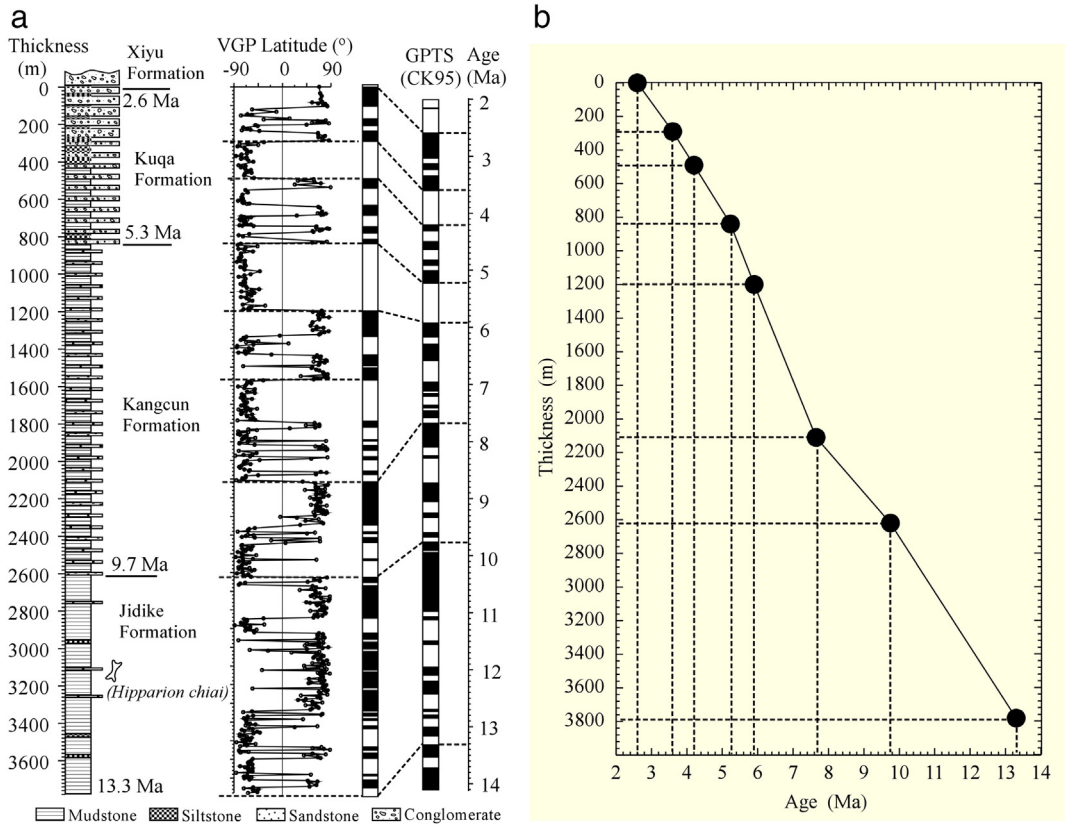

Fig. 4. (a) Magnetostratigraphy of the Kuchetawu study section (Sun et al., 2009a). Magnetic polarity is compared with the geological time scale of Cande and Kent (1995). (b) Age versus thickness based on magnetostratigraphic correlation.

4. Materials and methods

Although variations in sedimentary facies exist within the section (Fig. 3), the samples used for the following analysis were all from the intercalated lacustrine mudstone to fine siltstone beds. Therefore, the effects of variations in sedimentary facies on the following parameters are considered negligible.

The color index is a simple numerical expression that reflects the color of sediment. It has been used, to some extent, to infer past climatic changes (e.g., Yang and Ding, 2003; Spielvogel et al., 2004). The color index of 668 bulk samples was determined by using a Minolta-CM2002 spectrophotometer according to a method similar to that described by Yang and Ding (2003). For all samples, colorimeters of L* (lightness), a* (redness relative to greenness), and b* (yellowness relative to blueness) were used (Commission Internationale de l'Éclairage, 1978).

Analyses of soluble salts were performed on 161 bulk samples. Determination of soluble salts was undertaken in two steps: (1) water extraction at a soil:solution ratio of 1:5; and (2) measurement of the concentrations of cations (K^+, Na^+, Ca^{2+}, Mg^{2+}) in the extract using a PinAAcle 900F Atomic Absorption Spectrometer (uncertainty of less than 3%).

Analyses of total organic carbon (TOC) were performed on 169 samples using a LECO CS-344 Carbon/Sulfur Carbon Sulfur Determinator. Crushed samples (about 100 mg and 120 mesh) were heated to 1200 °C in an induction furnace after removing carbonate by using 5% hydrochloric acid (HCl).

Citrate-buffered dithionite (CBD)-extractable Fe (Fe_d), generally called free iron, was extracted following Mehra and Jackson (1960), subsequently measured by atomic absorption spectroscopy (AA). The total iron and K, Na, Ca, and Mg concentrations were determined by using Axios^{mAX}–Minerals XRF Spectrometer. Replicate analyses (n = 10) showed that uncertainties were below 5% for the above measurements.

5. Results

5.1. Long-term color variations and implications for climate change

The color results are given in the color-coordination system CIE (Commission Internationale de l'Éclairage) L*a*b*. The long-term variations in color parameters show the following trends (Fig. 5): (1) a general increasing trend of lightness and a decreasing trend of redness from 13.3 Ma to the end of the Pliocene; and (2) stepwise changes of both L* and a* occurred at ~7 Ma and ~5.3 Ma, while an increasing trend in b* only occurred after ~5.3 Ma. Data statistics indicate that the mean values of L* increased stepwise from 62.0 (n = 392) at 13.3–7 Ma to 66.6 (n = 142) and 69.6 (n = 121), after 7 and 5.3 Ma, respectively. In contrast to the increasing trends of L*, the mean values of redness decreased stepwise from 8.4 (n = 392) at 13.3–7 Ma to 5.0 (n = 142) and 4.2 (n = 121), after 7 and 5.3 Ma, respectively. Such changes in color index are closely linked to paleoenvironmental changes. The lightness of sediments or soils is thought to be affected by factors such as moisture content, organic matter concentration, and carbonate content (e.g., Schulze et al., 1993; Spielvogel et al., 2004). In this study, only dried samples were used; consequently, the effect of moisture content can be excluded. Lightness was found to be negatively correlated with organic matter content, while carbonate content may play a minor role in determining the lightness due to its lightening property (Spielvogel et al., 2004). Therefore, the stepwise trend of increasing lightness (Fig. 5a) can be partly attributed to a reduction in organic matter content. Given that organic matter content is influenced in part by biomass (Jenny, 1980), this suggests a decline in biomass driven by a drying climate, from the mid-Miocene to the end of the Pliocene. Sedimentary facies may also affect color indexes within a section; however, they are not deemed to be a dominant factor. For instance, the sedimentary facies characterized by alternations of ephemeral lakes and fluvial systems lasted from 9.7 to 5.3 Ma, demonstrating a

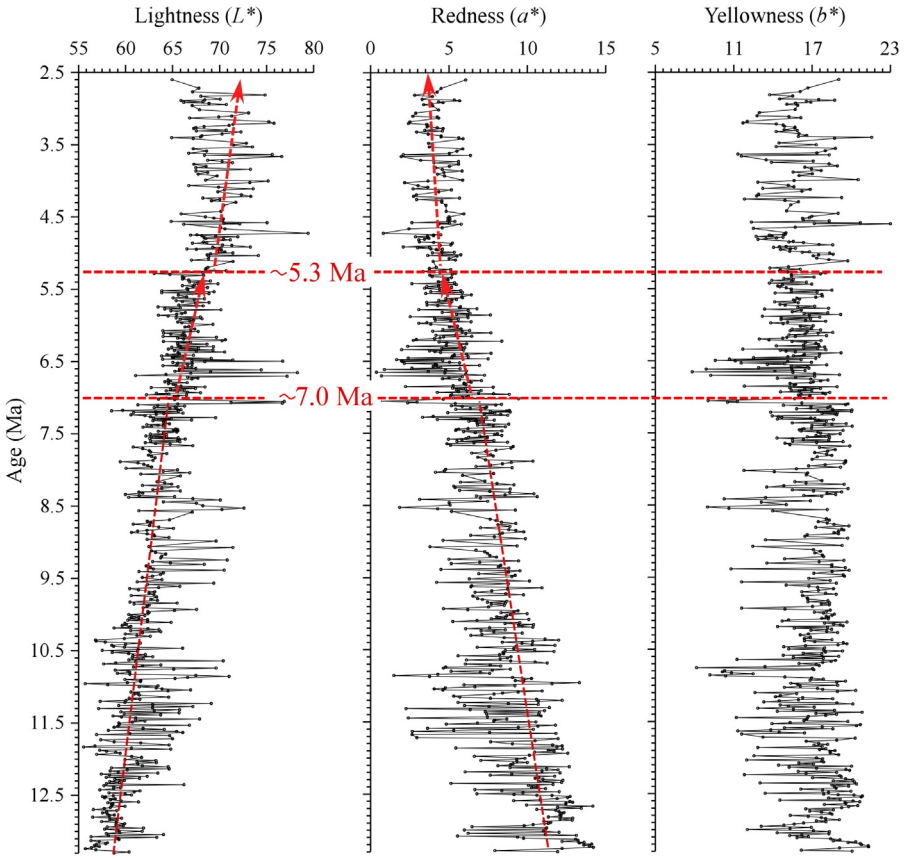

Fig. 5. Color index variations in the Kuchetawu section. Red arrows indicate the stepwise increase (lightness) or decrease (redness) trends commencing at ~7 Ma and ~5.3 Ma, respectively. (For interpretation of the references to color in this figure legend, the reader is referred to the web version of this article.)

long-term stable sedimentary environment and suggesting that the changes in the color indexes at ~7 Ma were not strongly governed by sedimentary facies.

The redness of sediments is associated with the amount of iron oxide released under chemical weathering (Walker, 1967), and is thus climate dependent. The redness curve displays a stepwise decreasing trend (Fig. 5b), implying a weakening in chemical weathering towards the end of the Pliocene.

In contrast to the parameters L* and a*, the yellowness of sediments does not show a prominent trend before 5.3 Ma (Fig. 5c). However, there is a slight increase thereafter. Yellowness also indicates the presence of iron oxides (Brady and Weil, 2000). Generally low soil temperatures do not favor the maturity of Fe forms; in such cases, poorly crystalline Fe hydroxides (e.g., goethite) rather than hematite (reddish color) appear, and this can at least partially account for the slightly increased trend of the yellowness after 5.3 Ma.

5.2. Variations in soluble salts and the inferred increase in aridity

Soluble salts are associated with authigenic evaporite minerals and usually occur in arid and semiarid regions. Vertical variations in soluble salts are an indicator of past salinity conditions and hydrological changes (Sinha and Raymahashay, 2004). Such variations have been extensively used to infer paleoclimatic fluctuations in many parts of the world (e.g., Wasson et al., 1984; Dean and Schwalb, 2000; Last and Vance, 2002; Sinha and Raymahashay, 2004). Fig. 6 shows a notable change in concentrations of soluble cations (Mg^{2+}, Ca^{2+}, Na^{+}, and K^{+}), indicated by generally higher values from ~7 Ma to 5.3 Ma. The increase in these soluble cations can be attributed partly to a drier climate with less leaching.

Many chemical indexes have been developed to indicate the extent of chemical weathering. Among them, the chemical index of alteration (CIA), proposed by Nesbitt and Young (1982), has been widely used (e.g., Price and Velbel, 2003; Clift et al., 2008). However, the CIA is most useful for silicate rocks, especially in the context of feldspar weathering, while other types of minerals are not necessarily reflected in this index. Retallack (1999, 2001) advocated a slightly different weathering index: the molecular ratio of bases to Al_2O_3, expressed as the molecular ratio of $(CaO + MgO + K_2O + Na_2O)/Al_2O_3$. Bases are easily leached during chemical weathering, whereas Al is resistant to chemical alteration; consequently, the bases/Al_2O_3 ratio has been used to characterize weathering intensity (e.g., Retallack, 1999; Retallack and Krull, 1999; Bestland, 2000; Sayyed and Hundekari, 2006). The bases/Al_2O_3 ratio of the present study section displays a general increasing trend after ~7 Ma, based on the major chemical compositions of the bulk samples, implying a weakening in chemical weathering since that time (Fig. 6e).

Finally, the above climatic events are supported by our previously compiled pollen record, which indicates that the warm-temperate broadleaf deciduous trees in this section declined after ~7 Ma (Zhang and Sun, 2011), mostly indicating a cooling climate (Fig. 6f).

5.3. Long-term fluctuations in TOC, Fe_d, Fe_p, and Fe_d/Fe_t

Patterns of total organic carbon (TOC) storage are critical for understanding climate change, given the importance of TOC for ecosystem processes (Trumbore et al., 1996). TOC is controlled by the balance of C inputs from plant production and outputs through decomposition (Schlesinger, 1977). Regional patterns of TOC are positively correlated with the mean annual precipitation, and are negatively correlated with the mean annual temperature (Oades, 1988).

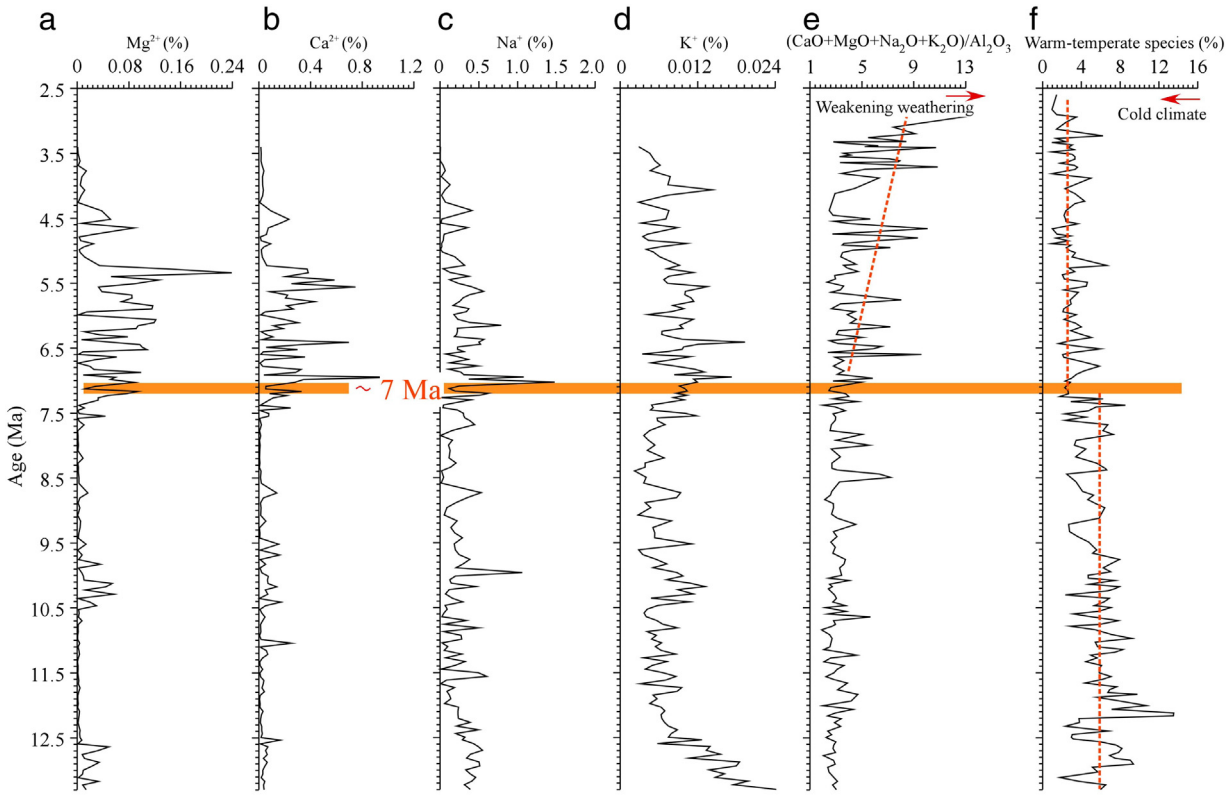

Fig. 6. Vertical variations in soluble cations at Kuchetawu (a–d) and their correlations with the chemical leaching index (bases/Al_2O_3) of bulk samples (e, higher values correspond to weaker chemical weathering), and the warm-temperate broadleaf deciduous species (f, higher percentages correspond to cooler climate).

In the present data, vertical fluctuations in TOC content indicate a general trend of decreasing TOC content since 13.3 Ma, with a sharper reduction occurring from ~5.3 Ma (Fig. 7a). As the palynological evidence indicates that the regional temperature of the study area tended to decrease since 13.3 Ma (Fig. 6f), the declining TOC values are unlikely to be due to enhanced decomposition, but rather to the

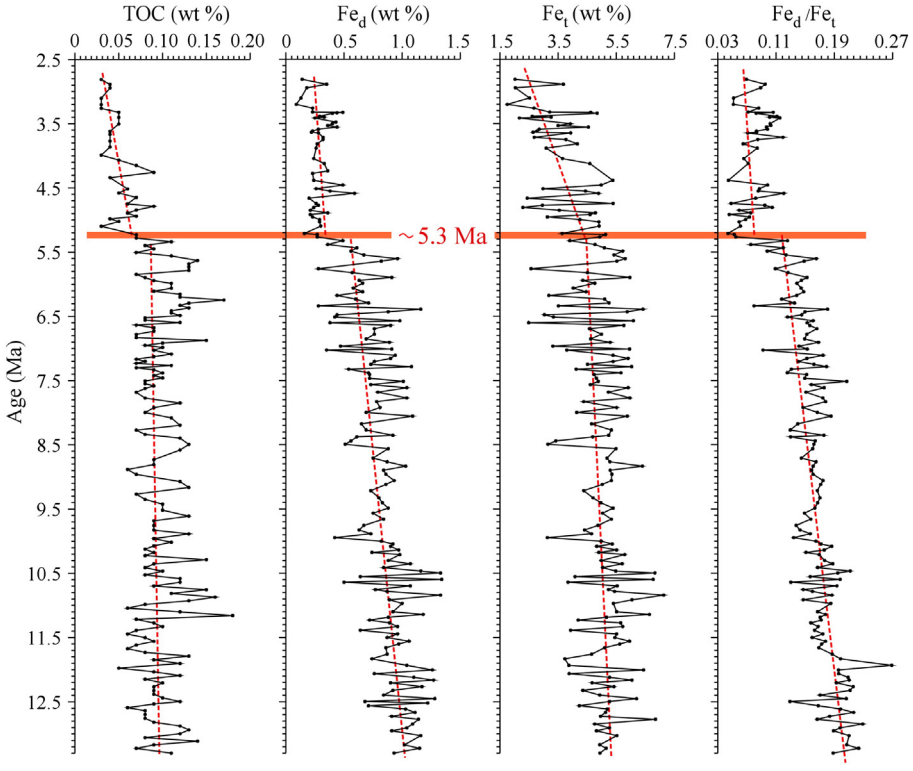

Fig. 7. Variations in the vertical concentrations of total organic carbon, CBD-Fe (Fe_d), total Fe (Fe_t), and Fe_d/Fe_t. A general decreasing trend is evident from 13.3 Ma, with a sharper decline occurring from ~5.3 Ma.

reduction of biomass as a result of a drying climate. In this context, the TOC variations reveal a drying regional climate, with this drying being particularly marked from ~5.3 Ma.

The above trends are similarly mirrored in iron parameters (Fig. 7). Iron is the second most abundant metal in the Earth's crust. The reactions of Fe in weathering processes are dependent largely on pH–Eh, and on the oxidation state of the Fe compounds involved. The sensitivity of Fe in sedimentary rocks to chemical alteration, and thus climate change, has resulted in iron oxides being comprehensively studied in paleoclimate reconstructions (Ding et al., 2001; Zhang et al., 2009).

Different parameters of Fe, including the citrate–bicarbonate–dithionite (CBD) extractable iron (Fe_d), the total iron (Fe_t), and Fe_d/Fe_t, have been used to study changes in climate. The free iron of Fe_d consists of pedogenic iron minerals such as ferrihydrite, goethite, and hematite (Dethier et al., 2012); hence, the content of Fe_d in sediments mainly reflects the degree of chemical weathering. In contrast to Fe_d, the total iron measures the entire Fe concentration. In general, oxidizing and alkaline conditions promote Fe precipitation in sedimentary rocks, and often lead to the formation of reddish coatings. The dominant reddish to brownish color of the study section indicates oxidizing conditions that are favorable for the precipitation of Fe when it is liberated from silicate weathering. In this context, the content of Fe_t within the section is at least partly controlled by chemical weathering. The ratio of Fe_d to Fe_t is a better chemical weathering index than either parameter by itself, as the ratio of the parameters can greatly serve to reduce the effect of changes in provenance on their individual concentrations. In summary, Fig. 7 reveals three trends: (1) all parameters display a general decreasing trend from 13.3 Ma to the end of the Pliocene; (2) a sharper decreasing trend is evident from ~5.3 Ma; and (3) the curves of Fe_d and the Fe_d/Fe_t are well correlated, demonstrating that they are better chemical weathering indexes than Fe_t alone. All three curves related to Fe indicate weakening chemical alteration from the mid-Miocene, especially after 5.3 Ma.

6. Discussion

The relationship between tectonic uplift and global climatic cooling during the Cenozoic has long been a focus of the study (e.g., Ruddiman and Kutzbach, 1989; Molnar and England, 1990; Raymo and Ruddiman, 1992; Zachos et al., 2001; Hay et al., 2002; Warny et al., 2003; Garcia-Castellanos, 2007; Retallack, 2007; Kohn and Fremd, 2008; Garcia-Castellanos and Villaseñor, 2011; Champagnac et al., 2012). To date, there has been debate concerning whether mountain uplift induces climatic cooling (Raymo and Ruddiman, 1992), or whether the late Cenozoic uplift is a consequence of climatic change (Molnar and England, 1990). The Tarim Basin in this study is surrounded by high Asian mountain systems, meaning its geophysical location is well suited for studying the forcing mechanisms of paleoclimatic change.

6.1. Regional tectonic history inferred from syntectonic growth strata during the late Miocene

It is important to understand the uplift history in a tectonically active region to better interpret climatic changes. In recent years, various techniques have been used to study the timing of tectonic uplift in mountains surrounding the Tarim Basin (e.g., Avouac et al., 1993; Sobel and Dumitru, 1997; Burchfiel et al., 1999; Charreau et al., 2006, 2008; Huang et al., 2006; Sobel et al., 2006; Hubert-Ferrari et al., 2007; Sun et al., 2008, 2009b; Sun and Zhang, 2009; Cao et al., 2013); however, the results are varied largely because the studies have addressed different problems with different methodologies at different times, and in consequence some are controversial. For instance, the traditional method for determining the onset of tectonic uplift is to examine the age of basal coarse conglomerates and/or the mass accumulation rate of Cenozoic sediments in a foreland basin (e.g., Métivier and Gaudemer, 1997; Yin et al., 1998; Ji et al., 2008); however, such sedimentary features are not linked solely to tectonics. For example, climate-related changes, such as enhanced frost weathering, can also account for the rapid accumulation of coarse sediments. Moreover, the above methods are highly dependent on the continuity of strata and the accuracy of age control; however, in the context of folding and thrusting within foreland basins, hiatuses are likely to exist.

Another commonly used method to determine the timing of onset of tectonic uplift is low-temperature thermochronology of apatite fission tracks (e.g., Hendrix et al., 1994; Sobel and Strecker, 2003; Sobel et al., 2006; Cao et al., 2013). This technique constrains the timing of the onset of cooling, which is assumed to be linked to exhumation driven by crustal shortening. However, results vary across different studies. For instance, Sobel et al. (2006) reported significant exhumation of the southwest Tian Shan in the late Oligocene–Miocene, whereas Cao et al. (2013) argued that exhumation of the Eastern Pamir domes occurred since 6–5 Ma and may have accelerated at ~3–1 Ma.

Recently, rock magnetic characteristics (anisotropy of magnetic susceptibility, AMS) have also been used to infer tectonic uplift (Charreau et al., 2006; Huang et al., 2006; Tang et al., 2012). However, AMS is affected by many factors including sedimentary compaction, sedimentary facies, texture of sediments, source materials, and tectonic compression. Thus, AMS is not solely controlled by tectonics, and care must be taken when only using AMS data to identify periods of tectonic uplift.

In contrast to the above methods, deposition in active tectonic settings is always controlled by growing structures. The syntectonic sedimentation (growth strata) is contemporaneous with tectonic deformation in active fold-and-thrust zones in front of orogenic belts (e.g., Suppe et al., 1992, 1997; Vergés et al., 2002; Cunningham et al., 2003). In this context, the chronology of syntectonic sediments, associated with a natural growth fold, can be a valuable tool for understanding the interplay between sedimentation and tectonic activity (Masaferro et al., 2002).

In recent years, growth strata in the foreland basins of the Tian Shan and Kunlun mountains have been well studied (Hubert-Ferrari et al., 2007; Sun et al., 2008, 2009b; Sun and Zhang, 2009). The results indicate that growth strata began to form at ~7–5 Ma and lasted until the early Pleistocene (Fig. 8). Therefore, although the collision of India with Eurasia occurred as early as 55–50 Ma (Molnar and Tapponnier, 1975), the intracontinental deformation of the Tian Shan range in response to this collision occurred much later, spanning a time interval from the latest Miocene to the early Pleistocene.

In addition to the tectonics in the Tian Shan range, there have been more regional records for this delay in Inner Asia to the early India–Eurasia collision. In the Gobi Altai orogen, limited Paleogene strata throughout the Gobi Corridor region suggest that from the Late Cretaceous until the mid-late Miocene, the entire region was tectonically quiescent and eroded down to a low-relief and peneplained landscape until Late Miocene–Recent reactivation (Cunningham et al., 2003). In the Qilian Shan and associated ranges on the northeastern margin of the Tibetan Plateau, early workers held that tectonic uplift was largely confined to the late Miocene and Pliocene (e.g., Burchfiel et al., 1989; Meyer et al., 1998; Tapponnier et al., 2001). Such views were corroborated by considerable later evidence for mountain building throughout the northeastern Tibetan Plateau during the late Miocene (e.g., Fang et al., 2005; Zheng et al., 2006, 2010a,b; Lease et al., 2007).

6.2. Forcing mechanism of stepwise aridification since the late Miocene

To discuss the forcing mechanism of stepwise aridification since the late Miocene, we correlate the regional climate record of the Tarim Basin with the global deep sea record and regional tectonic uplift events (Fig. 9).

The increasing contents of soluble cations in evaporite minerals (Fig. 9a) indicate a peak at ~7–5.3 Ma. For which, we have two interpretations. Firstly, it has been broadly accepted that thick evaporite successions beneath the floor of the Mediterranean, led to the Messinian

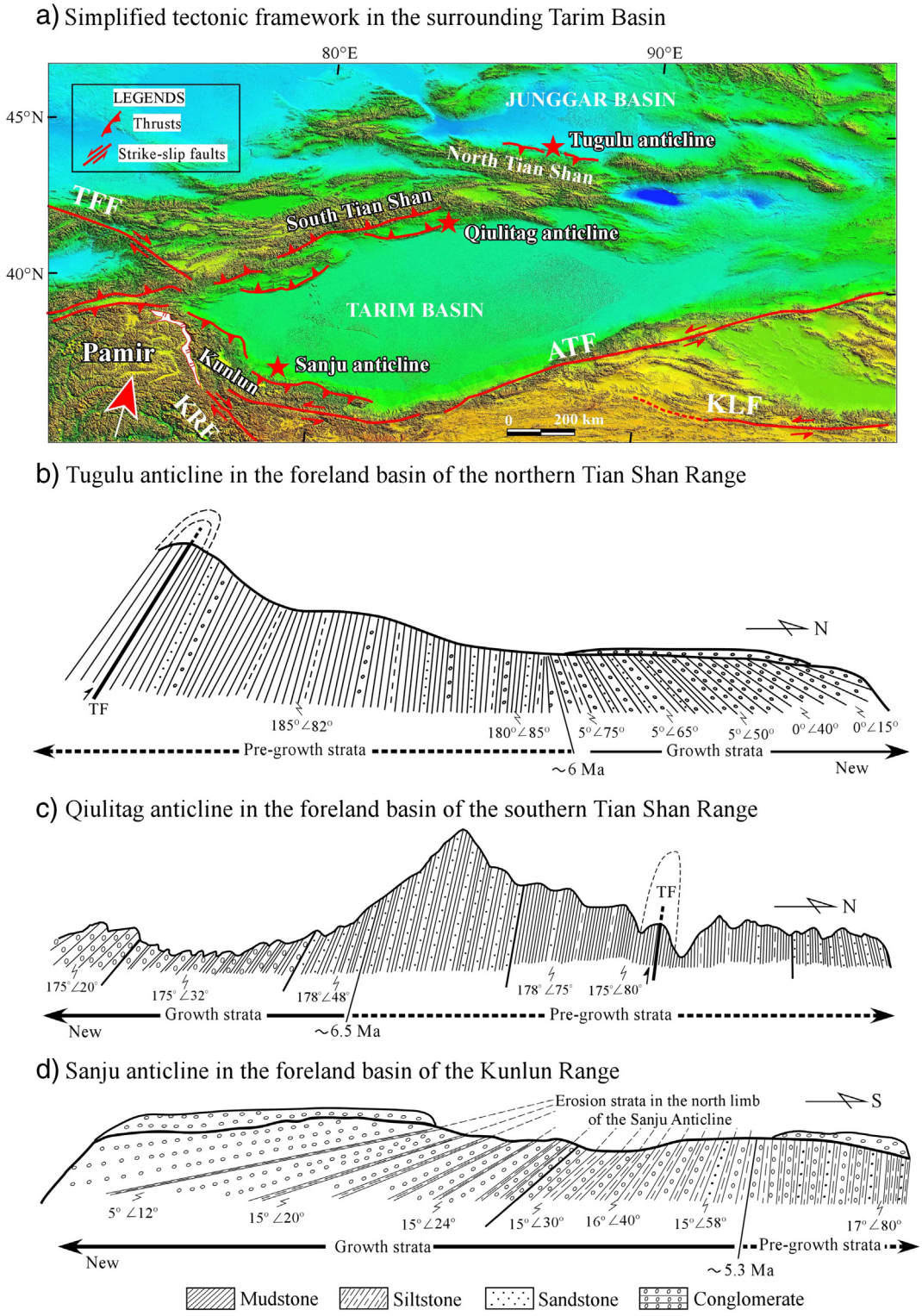

Fig. 8. Syntectonic growth strata indicating crustal shortening and mountain uplift from ~7–5 Ma. (a) Digital elevation model showing a simplified tectonic framework and the locations of anticlines in the fold-and-thrust foreland basins. The red arrow indicates the direction of northward indentation of the Pamir salient related to the India–Eurasia convergence. ATF: Altyn Tagh Fault, KLF: Kunlun Fault; TTF: Talas–Fergana Fault; KRF: Karakoram Fault. (b) Tugulu Anticline in the foreland basin of the northern Tian Shan, showing syntectonic growth strata initiated at ~6 Ma (Sun and Zhang, 2009). (c) Growth strata in the Qiulitag Anticline in the foreland basin of the southern Tian Shan initiated at ~6.5 Ma (modified from Sun et al., 2009a). (d) Growth strata in the Sanju Anticline in the foreland basin of the Kunlun range initiated at ~5.3 Ma (Sun et al., 2008). (For interpretation of the references to color in this figure legend, the reader is referred to the web version of this article.)

Salinity Crisis during the latest Miocene (Hsü et al., 1973) that was caused by tectonically induced uplift of the Strait of Gibraltar, which isolated the Mediterranean from the Atlantic, in response to the convergence between the Arabian Plate and Eurasia (e.g., Hsü and Bernoulli, 1978; Krijgsman et al., 1999; Garcia-Castellanos and Villaseñor, 2011). To date, controversies still exist about the timing and duration of this event. Although some authors suggested an age of 5.96–5.33 Ma (e.g., Krijgsman et al., 1999), others assigned an age of 6.8–5.3 Ma

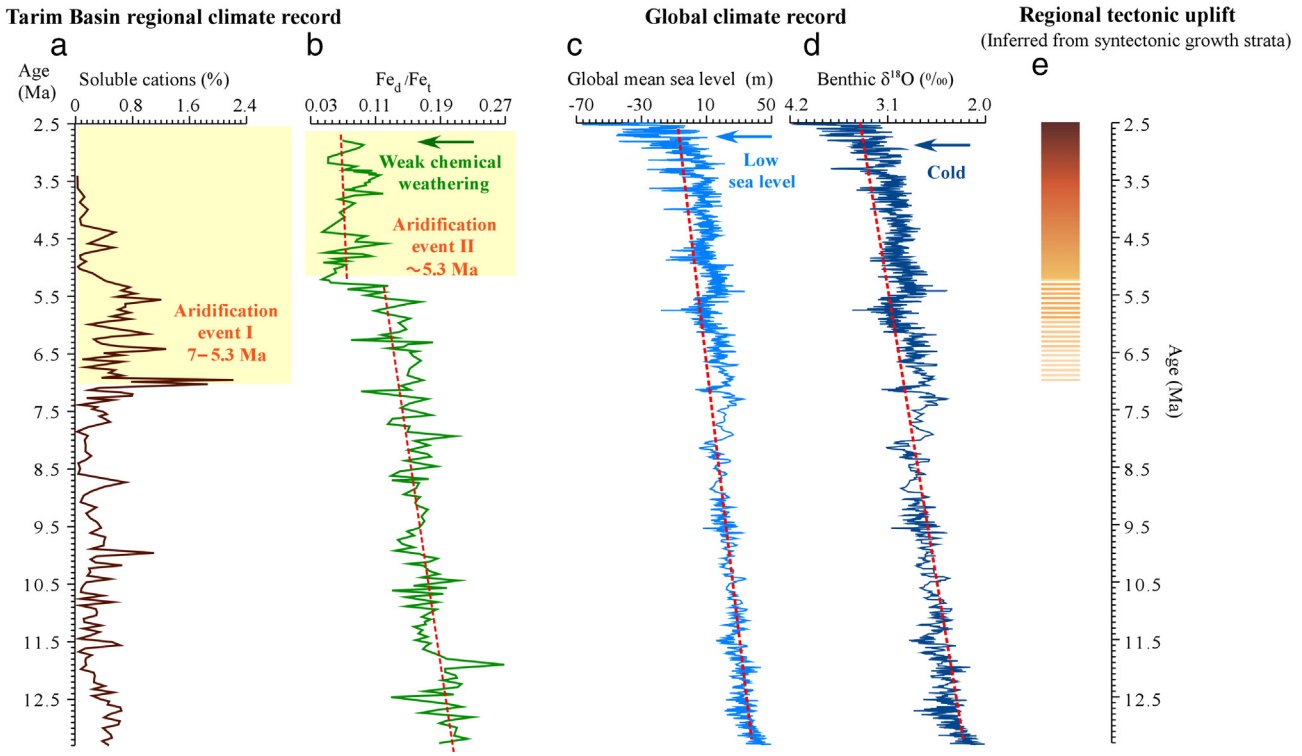

Fig. 9. Regional climate change in the Tarim Basin (a, b) is correlated with global climate records (c, d) and regional tectonic uplift events (e). Soluble cations include Ca^{2+}, Mg^{2+}, Na^{+}, and K^{+}; sea level data are from Hansen et al. (2013); oxygen isotopic data for 0–5.32 Ma and 5.32–13.3 Ma are from Lisiecki and Raymo (2005) and Zachos et al. (2001), respectively.

(e.g., Butler et al., 1999; Warny et al., 2003). This later time range is consistent with the high peak of soluble cations of Fig. 9a. We note that although the Pamir orogen collides with the South Tian Shan orogen in response to the convergence between India and Eurasia (Fig. 1), they were at least 300–400 km apart before the early collision of India–Eurasia at ~55–50 Ma (e.g., Burtman and Molnar, 1993). Northward displacement of the Pamir arc has happened at least since the early Eocene (Burtman and Molnar, 1993). The contemporaneity between the high peak of the soluble cations of evaporite minerals in the Tarim Basin and the duration of the Messinian Salinity Crisis suggests that there was a close link between them. The Tarim Basin lies in the downwind direction of the Mediterranean Sea and there would exist a narrow gateway between the Tian Shan orogen and the Pamir salient at 7–5.3 Ma, which was thus favorable for the transportation of evaporite minerals from the dried-up Mediterranean to the Tarim Basin (Fig. 10a). Secondly, due to the shrinkage of the Mediterranean Sea, vapor transportation by westerlies was greatly reduced, and this led to aridification in the downwind Tarim Basin. The second case is supported by the weak chemical weathering indicated by the decline of redness at 7–5.3 Ma (Fig. 5b), as well as by the early existence of limited eolian sand dunes in the interior of the Tarim Basin (Sun et al., 2009b). However, the extent of this early episode of aridification was much less than that of the later aridification event that was initiated 5.3 Ma, because extensive sand dunes similar to those in the present desert of the Tarim Basin formed at 5.3 Ma (Sun and Liu, 2006). This early phase of aridification is not mirrored by global-scale climatic records of the fluctuation of sea-level (Fig. 9c) and of marine oxygen isotopes (Fig. 9d). In this context, a regional tectonic factor played a significant role in the first phase of aridification in the Tarim Basin (Fig. 9e).

The chemical weathering index, represented by Fe_d/Fe_t, presents another means of assessing the weakening alteration and drying climate since ~5.3 Ma (Fig. 9b). The extent of this second aridification event, which far exceeded the earlier one, is supported by the formation of large-scale dune fields (Sun and Liu, 2006), and by the long-core record in the Tarim Basin (Liu et al., 2014). As discussed above, syntectonic growth folding lasted from 7 or 5.3 Ma to the end of the early Pleistocene (Fig. 9e), and this was accompanied by the accumulation of higher energy alluvial and fluvial coarse conglomerates after 5.3 Ma, this implying intense tectonic uplift. After 5.3 Ma, sea water entered the Mediterranean as a result of the erosion or collapse of the Gibraltar isthmus (Fig. 10b). Although the area of sea was much larger compared with that during the Messinian Salinity Crisis (Fig. 10b), there was enhanced aridity in the downwind Tarim Basin. This can be explained by the ongoing northward indentation of the Pamir orogen, which mostly collided with the Tian Shan orogen at 5.3 Ma (Fig. 10b). This caused uplift of the surrounding mountains, and blocked the transport of water vapor from the upwind Mediterranean Sea and the Paratethys, leading to the extreme aridity in the Tarim Basin since 5.3 Ma.

Similar to the first aridification event at 7–5.3 Ma, this later aridification phase cannot be matched with the global-scale climatic records of sea-level (Fig. 9c) and marine oxygen isotopes (Fig. 9d). Therefore, regional tectonics played a dominant role in driving this second aridification event, whereas global cooling that induced sea-level decline, only played a minor role.

Although the two regional aridification events are not mirrored by the global climatic curves during the latest Miocene, the long-term trend of a reduction in chemical weathering, as revealed by Fe_d/Fe_t, is generally correlated with a global sea level fall (Fig. 9b), as well as a long-term cooling trend revealed by high-latitude climate reconstructions from the marine oxygen isotopic record of the past 13.3 Ma (Fig. 9d). This suggests that the general trend of regional climatic drying in the Tarim Basin was controlled by first-order global cooling, whereas the two stepwise aridification events in the latest Miocene were predominantly controlled by regional tectonic uplift as a response of the intracontinental deformation of the India–Eurasia collision in Inner Asia. In the last case global cooling only played a minor role.

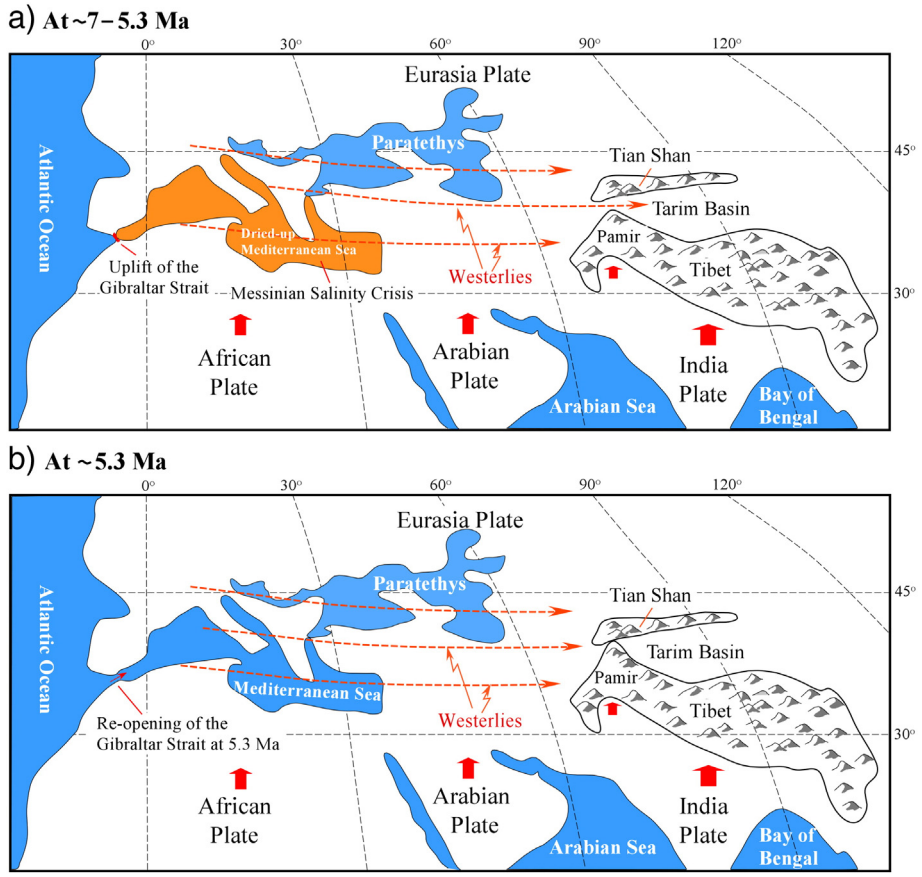

Fig. 10. Schematic maps showing the relationship between regional tectonics, wind patterns, and paleoclimate during the latest Miocene. The geographic location of the Paratethys was referred from Popov et al. (2004). (a) Regimes of sea distribution, extent of the dried-up Mediterranean Sea, and the positions of the Pamir and Tian Shan orogens. Note that there was probably a narrow gap between them permitting the transport of evaporite minerals from the desiccated Mediterranean to the Tarim Basin from ~7 to 5.3 Ma. The dried-up Mediterranean Sea also resulted in reduced vapor transport downwind to the Tarim Basin. (b) The northward indentation of the Pamir salient finally led to the collision with the Tian Shan orogen at ~5.3 Ma, together with the uplift of the surrounding mountains, blocking vapor transport by the westerlies to the Tarim Basin, which caused much enhanced aridification. The red solid arrows indicate the directions of northward plate movements. (For interpretation of the references to color in this figure legend, the reader is referred to the web version of this article.)

7. Conclusions

The Tarim Basin is the largest inland basin in the Asian interior, and it is home to the Taklimakan Desert. Analysis of the Kuchetawu section in the northern Tarim Basin allowed us to reconstruct the long-term history of aridity and to explore the interplay between regional tectonic uplift and climatic change in an active tectonic region.

Based on multiple geochemical parameters, we reconstructed high-resolution paleoclimatic trends spanning the period from 13.3 to 2.5 Ma. The data reveal a general trend towards a cold–dry climate with the initiation of stepwise aridification at ~7–5.3 Ma and after ~5.3 Ma. The correlation between climatic and tectonic events leads us to propose that the general long-term drying trend since 13.3 Ma was a response to global climatic cooling, while the stepwise aridification that commenced since the latest Miocene was mainly controlled by regional tectonic uplift.

Acknowledgments

This work was supported by the "Strategic Priority Research Program" of the Chinese Academy of Sciences (XDB03020500), the National Basic Research Program of China (2013CB956400), and the National Nature Science Foundation of China (Grants 41290251 and 41272203). We thank Dr. Zhenqing Zhang for his assistance in field sampling, He Li and Jie Cao for their assistance in data measurement.

References

Avouac, J.P., Tapponnier, P., Bai, M., Hou, Y., Wang, G., 1993. Active thrusting and folding along the northeastern Tienshan, and rotation of Tarim relative to Dzungaria and Kazakhstan. J. Geophys. Res. 98, 6755–6804.

Bestland, E.A., 2000. Weathering flux and CO_2 consumption determined from palaeosol sequences across the Eocene–Oligocene transition. Palaeogeogr. Palaeoclimatol. Palaeoecol. 156, 301–326.

Bosboom, R., Dupont-Nivet, G., Grothe, A., Brinkhuis, H., Villa, G., Mandic, O., Stoica, M., Huang, W., Yang, W., Guo, Z., Krijgsman, W., 2013. Linking Tarim Basin sea retreat (west China) and Asian aridification in the late Eocene. Basin Res. 26, 1–20.

Bosboom, R.E., Abels, H.A., Hoorn, C., van den Berg, B.C.J., Guo, Z., Dupont-Nivet, G., 2014. Aridification in continental Asia after the Middle Eocene Climatic Optimum (MECO). Earth Planet. Sci. Lett. 389, 34–42.

Brady, N.C., Weil, R.R., 2000. Elements of the Nature and Properties of Soils. Prentice Hall, Upper Saddle River, New Jersey.

Burchfiel, B.C., Deng, Q., Molnar, P., Royden, L.H., Wang, Y., Zhang, P., Zhang, W., 1989. Intracrustal detachment within zones of continental deformation. Geology 17, 448–452.

Burchfiel, B.C., Brown, E.T., Deng, Q.D., Feng, X.Y., Li, J., Molnar, P., Shi, J.B., Wu, Z.M., You, H.C., 1999. Crustal shortening on the margins of the Tien Shan, Xinjiang, China. Int. Geol. Rev. 41, 665–700.

Burtman, V.S., Molnar, P., 1993. Geological and geophysical evidence for deep subduction of continental crust beneath the Pamir. Geol. Soc. Am. Spec. Pap. 281, 1–76.

Butler, R.W.H., McClelland, E., Jones, R.E., 1999. Calibrating the duration and timing of the Messinian salinity crisis in the Mediterranean: linked tectonoclimatic signals in thrust-top basins of Sicily. J. Geol. Soc. Lond. 156, 827–835.

Cande, S.C., Kent, D.V., 1995. Revised calibration of the geomagnetic polarity timescale for the Late Cretaceous and Cenozoic. J. Geophys. Res. 100, 6093–6095.

Cao, K., Bernet, M., Wang, G.C., van der Beek, P., Wang, A., Zhang, K.X., Enkelmann, E., 2013. Focused Pliocene–Quaternary exhumation of the Eastern Pamir domes, western China. Earth Planet. Sci. Lett. 363, 16–26.

Champagnac, J.-D., Molnar, P., Sue, C., Herman, F., 2012. Tectonics, climate, and mountain topography. J. Geophys. Res. 117, B02403. http://dx.doi.org/10.1029/2011JB008348.

Chang, H., An, Z.S., Liu, W.G., Qiang, X.K., Song, Y.G., Ao, H., 2012. Magnetostratigraphic and paleoenvironmental records for a Late Cenozoic sedimentary sequence drilled from Lop Nor in the eastern Tarim Basin. Global Planet. Chang. 80–81, 113–122.
Charreau, J., Gilder, S., Chen, Y., Dominguez, S., Avouac, J.P., Sen, S., Jolivet, M., Li, Y., Wang, W., 2006. Magnetostratigraphy of the Yaha section, Tarim Basin (China): 11 Ma acceleration in erosion and uplift of the Tian Shan mountains. Geology 34, 181–184.
Charreau, J., Chen, Y., Gilder, S., Barier, L., 2008. Comment on "Magnetostratigraphic study of the Kuche Depression, Tarim Basin, and Cenozoic uplift of the Tian Shan Range, Western China". Earth Planet. Sci. Lett. 268, 325–329.
Clift, P.D., Hodges, K.V., Heslop, D., Hannigan, R., Long, H.V., Calves, G., 2008. Correlation of Himalayan exhumation rates and Asian monsoon intensity. Nat. Geosci. 1, 875–880.
Commission Internationale de L'Éclairage (CIE), 1978. Recommendations on Uniform Color Spaces—Color-difference Equations, Psychometric Color Terms. CIE, Paris (Publ. 15, Suppl. 2).
Cunningham, D., Owen, L.A., Snee, L.W., Li, J., 2003. Structural framework of a major intracontinental orogenic termination zone: the easternmost Tien Shan, China. J. Geol. Soc. London 160, 575–590.
Dean, W.E., Schwalb, A., 2000. Holocene environmental and climatic change in the Northern Great Plains as recorded in the geochemistry of sediments in Pickerel Lake, South Dakota. Quat. Int. 67, 5–20.
Deng, T., 2006. Chinese Neogene mammal biochronology. Vertebr. PalAsiatic 44, 143–163.
Deng, Q.D., Feng, X.Y., Zhang, P.Z., Xu, X.W., Yang, X.P., Peng, S.Z., Li, J., 2000. Active Tectonics of the Tianshan Mountains. Seismology Press, Beijing.
Dethier, D.P., Birkeland, P.W., McCarthy, J.A., 2012. Using the accumulation of CBD-extractable iron and clay content to estimate soil age on stable surfaces and nearby slopes, Front Range, Colorado. Geomorphology 173–174, 17–29.
Ding, Z.L., Yang, S.L., Sun, J.M., Liu, T.S., 2001. Iron geochemistry of loess and red clay deposits in the Chinese Loess Plateau and implications for long-term Asian monsoon evolution in the last 7.0 Ma. Earth Planet. Sci. Lett. 185, 99–109.
Dong, X.X., Ding, Z.L., Yang, S.L., Luo, P., Wang, X., Ji, J.L., 2013. Synchronous drying and cooling in central Asia during late Oligocene. Chin. Sci. Bull. 58, 3119–3124.
Dupont-Nivet, G., Krijgsman, W., Langereis, C.G., Abels, H.A., Dai, S., Fang, X., 2007. Tibetan Plateau aridification linked to global cooling at the Eocene–Oligocene transition. Nature 445, 635–638.
Fang, X.M., Lü, L.Q., Yang, S.L., Li, J.J., An, Z.S., Jiang, P.A., Chen, X.L., 2002. Loess in Kunlun Mountains and its implications on desert development and Tibetan Plateau uplift in west China. Sci. China Ser. D 45, 289–299.
Fang, X., Yan, M., Van der Voo, R., Rea, D.K., Song, C., Pares, J.M., Gao, J., Nie, J., Dai, S., 2005. Late Cenozoic deformation and uplift of the NE Tibetan Plateau: evidence from high-resolution magnetostratigraphy of the Guide Basin, Qinghai Province China. Geol. Soc. Am. Bull. 117, 1208–1225.
Fu, B.H., Lin, A.M., Kano, K., Maruyama, T., Guo, J.M., 2003. Quaternary folding of the eastern Tianshan, Northwest China. Tectonophysics 369, 79–101.
Fu, B.H., Ninomiya, Y., Guo, J.M., 2010. Slip partitioning in the northeast Pamir–Tian Shan convergence zone. Tectonophysics 483, 344–364.
Garcia-Castellanos, D., 2007. The role of climate during high plateau formation: insights from numerical experiments. Earth Planet. Sci. Lett. 257, 372–390.
Garcia-Castellanos, D., Villaseñor, A., 2011. Messinian salinity crisis regulated by competing tectonics and erosion at the Gibraltar arc. Nature 480, 359–363.
Hansen, J., Sato, M., Russell, G., Kharecha, P., 2013. Climate sensitivity, sea level and atmospheric carbon dioxide. Phil. Trans. R. Soc. A 371, 20120294. http://dx.doi.org/10.1098/rsta.2012.0294.
Hay, W.W., Soeding, E., DeConto, R.M., Wold, C.N., 2002. The Late Cenozoic uplift — climate change paradox. Int. J. Earth Sci. 91, 746–774.
Hendrix, M.S., Dumitru, T.A., Graham, S.A., 1994. Late Oligocene-early Miocene unroofing in the Chinese Tian Shan: an early effect of the India–Asia collision. Geology 22, 487–490.
Hoorn, C., Straathof, J., Abels, H.A., Xu, Y., Utescher, T., Dupont-Nivet, G., 2012. A Late Eocene palynological record of climate change and Tibetan Plateau uplift (Xining Basin, China). Palaeogeogr. Palaeoclimatol. Palaeoecol. 344–345, 16–38.
Hsü, K.J., Bernoulli, D., 1978. Genesis of the Tethys and the Mediterranean. Init. Rep. DSDP 42, 943–950.
Hsü, K.J., Ryan, W.B.F., Cita, M.B., 1973. Late Miocene desiccation of the Mediterranean. Nature 242, 240–244.
Huang, B.C., Piper, J.D.A., Peng, S.T., Liu, T., Li, Z., Wang, Q.C., Zhu, R.X., 2006. Magnetostratigraphic study of the Kuche Depression, Tarim Basin, and Cenozoic uplift of the Tian Shan Range, Western China. Earth Planet. Sci. Lett. 251, 346–364.
Hubert-Ferrari, A., Suppe, J., Gonzalez-Mieres, R., Wang, X., 2007. Mechanisms of active folding of the landscape (southern Tian Shan, China). J. Geophys. Res. 112, B03S09. http://dx.doi.org/10.1029/2006JB004362.
Jenny, H., 1980. The soil resource. Ecological Studies. Springer, Verlag, N.Y., p. 37.
Ji, J.L., Luo, P., White, P., Jiang, H.C., Gao, L., Ding, Z.L., 2008. Episodic uplift of the Tianshan Mountains since the late Oligocene constrained by magnetostratigraphy of the Jingou River section, in the southern margin of the Junggar Basin, China. J. Geophys. Res. 113, B05102. http://dx.doi.org/10.1029/2007JB005064.
Kohn, M.J., Fremd, T.J., 2008. Miocene tectonics and climate forcing of biodiversity, western United States. Geology 36, 783–786.
Krijgsman, W., Hilgen, F.J., Raffi, I., Sierro, F.J., Wilson, D.S., 1999. Chronology, causes and progression of the Messinian salinity crisis. Nature 400, 652–655.
Kutzbach, J.E., Guetter, P.J., Ruddiman, W.F., Prell, W.L., 1989. Sensitivity of climate to late Cenozoic uplift in southern Asia and the American west, numerical experiments. J. Geophys. Res. 94, 18393–18407.
Last, W.M., Vance, R.E., 2002. The Holocene history of Oro Lake, one of the western Canada's longest continuous lacustrine records. Sediment. Geol. 148, 161–184.
Lease, R.O., Burbank, D.W., Gehrels, G., Wang, Z., Yuan, D., 2007. Signatures of mountain building: detrital zircon U/Pb ages from northeastern Tibet. Geology 35, 239–242.
Lisiecki, L.E., Raymo, M.E., 2005. A Pliocene–Pleistocene stack of 57 globally distributed benthic $\delta^{18}O$ records. Paleoceanography 20, PA1003. http://dx.doi.org/10.1029/2004PA001071.
Liu, X.D., Kutzbach, J.E., Liu, Z.Y., An, Z.S., Li, L., 2003. The Tibetan Plateau as amplifier of orbital scale variability of the East Asian monsoon. Geophys. Res. Lett. 30, 1839. http://dx.doi.org/10.1029/2003GL017510.
Liu, W.G., Liu, Z.H., An, Z.S., Sun, J.M., Chang, H., Wang, N., Dong, J.B., Wang, H.Y., 2014. Late Miocene episodic lakes in the arid Tarim Basin, western China. Proc. Natl. Acad. Sci. U. S. A. 111, 16292–16296.
Lu, H.Y., Wang, X., Li, L., 2010. Aeolian sediment evidence that global cooling has driven late Cenozoic stepwise aridification in central Asia. Geol. Soc. London Spec. Publ. 342, 29–44.
Manabe, S., Broccoli, A.J., 1990. Mountains and arid climates of middle latitudes. Science 247, 192–194.
Manabe, S., Terpstra, T.B., 1974. The effects of mountains on the general circulation of the atmosphere as identified by numerical experiments. J. Atmos. Sci. 31, 3–42.
Masaferro, J.L., Bulnes, M., Poblet, J., Eberli, G.P., 2002. Episodic folding inferred from syntectonic carbonate sedimentation: the Santaren anticline, Bahamas foreland. Sediment. Geol. 146, 11–24.
Mehra, O.P., Jackson, M.L., 1960. Iron oxide removal from soils and clays by a dithionite–citrate system buffered with sodium bicarbonate. Clays Clay Minerals 7, 317–327.
Métivier, F., Gaudemer, Y., 1997. Mass transfer between eastern Tien Shan and adjacent basins (central Asia): constraints on regional tectonics and topography. Geophys. J. Int. 128, 1–17.
Meyer, B., Tapponnier, P., Bourjot, L., Métivier, F., Gaudemer, Y., Peltzer, G., Shunmin, G., Zhitai, C., 1998. Crustal thickening in Gansu–Qinghai, lithospheric mantle subduction, and oblique, strike-slip controlled growth of the Tibet Plateau. Geophys. J. Int. 135, 1–47.
Miao, Y.F., Fang, X.M., Herrmann, M., Wu, F.L., Liu, D.L., 2011. Miocene pollen record of KC-1 core in the Qaidam Basin, NE Tibetan Plateau and implications for evolution of the East Asian monsoon. Palaeogeogr. Palaeoclimatol. Palaeoecol. 299, 30–38.
Miao, Y.F., Herrmann, M., Wu, F.L., Yan, X.L., Yang, S.L., 2012. What controlled Mid-late Miocene long-term aridification in Central Asia? — global cooling or Tibetan Plateau uplift: a review. Earth Sci. Rev. 112, 155–172.
Miao, Y.F., Fang, X.M., Wu, F.L., Cai, M.T., Song, C.H., Meng, Q.Q., Xu, L., 2013. Late Cenozoic continuous aridification in the western Qaidam Basin: evidence from sporopollen records. Clim. Past 9, 1485–1508.
Molnar, P., England, P., 1990. Late Cenozoic uplift of mountain ranges and global climate change: chicken or egg? Nature 346, 29–34.
Molnar, P., Tapponnier, P., 1975. Cenozoic tectonics of Asia: effects of a continental collision. Science 189, 419–426.
Nesbitt, H.W., Young, G.M., 1982. Early Proterozoic climates and plate motions inferred from major element chemistry of lutites. Nature 299, 715–717.
Oades, J.M., 1988. The retention of organic matter in soils. Biogeochemistry 5, 33–70.
Popov, S.V., Rögl, F., Rozanov, A.Y., Steininger, F.F., Shcherba, I.G., Kovac, M., 2004. Lithological–Paleogeographic maps of Paratethys 10 Maps Late Eocene to Pliocene. Cour. Forsch.-Inst. Senckenberg. 250, 1–46.
Price, J.R., Velbel, M.A., 2003. Chemical weathering indices applied to weathering profiles developed on heterogeneous felsic metamorphic parent rocks. Chem. Geol. 202, 397–416.
Ramstein, G., Fluteau, F., Besse, J., Joussaume, S., 1997. Effect of orogeny, plate motion and land-sea distribution on Eurasian climate change over the past 30 million years. Nature 386, 788–795.
Raymo, M.E., Ruddiman, W.F., 1992. Tectonic forcing of late Cenozoic climate change. Nature 359, 117–122.
Retallack, G.J., 1999. Post-apocalyptic greenhouse paleoclimate revealed by earliest Triassic paleosols in the Sydney Basin, Australia. Geol. Soc. Am. Bull. 111, 52–70.
Retallack, G.J., 2001. Soils of the Past. Blackwell, Oxford.
Retallack, G.J., 2007. Cenozoic Paleoclimate on Land in North America. J. Geol. 115, 271–294.
Retallack, G.J., Krull, E.S., 1999. Landscape ecological shift at the Permian–Triassic boundary in Antarctica. Aust. J. Earth Sci. 46, 785–812.
Ruddiman, W.F., Kutzbach, J.E., 1989. Forcing of the late Cenozoic uplift Northern Hemisphere climate by plateau uplift in the Southern Asia and American West. J. Geophys. Res. 94, 18409–18427.
Sayyed, M.R., Hundekari, S.M., 2006. Preliminary comparison of ancient bole beds and modern soils developed upon the Deccan volcanic basalts around Pune (India): potential for paleoenvironmental reconstruction. Quat. Int. 156–157, 189–199.
Schlesinger, W.H., 1977. Carbon balance in terrestrial detritus. Ann. Rev. Ecol. Syst. 8, 51–81.
Schulze, D.G., Nagel, J.L., van Scoyoc, G.E., Henderson, T.L., Baumgardner, M.F., Stott, D.E., 1993. Significance of organic matter in determining soil colors. In: Bigham, J.M., Ciolkosz, E.J. (Eds.), Soil Color. Soil Sci. Soc. Am. Spec. Publ. 31, pp. 71–90 (Madison).
Sinha, R., Raymahashay, B.C., 2004. Evaporite mineralogy and geochemical evolution of the Sambhar Salt Lake, Rajasthan, India. Sediment. Geol. 166, 59–71.
Sobel, E.R., Dumitru, T.A., 1997. Thrusting and exhumation around the margins of the western Tarim Basin during the India–Asia collision. J. Geophys. Res. 102, 5043–5063.
Sobel, E.R., Strecker, M.R., 2003. Uplift, exhumation, and precipitation: tectonic and climatic control of Late Cenozoic landscape evolution in the northern Sierras Pampeanas, Argentina. Basin Res. 15 http://dx.doi.org/10.1046/j.1365-2117.2003.00214.x.
Sobel, E.R., Chen, J., Heermance, R.V., 2006. Late Oligocene–Early Miocene initiation of shortening in the Southwestern Chinese Tian Shan: implications for Neogene shortening rate variations. Earth Planet. Sci. Lett. 247, 70–81.
Spielvogel, S., Knicker, H., Kogel-Knabner, I., 2004. Soil organic matter composition and soil lightness. J. Plant Nutr. Soil Sci. 167, 545–555.

Sun, J.M., Liu, T.S., 2006. The age of the Taklimakan Desert. Science 312, 1621.
Sun, J.M., Zhang, Z.Q., 2009. Syntectonic growth strata and implications for late Cenozoic tectonic uplift in the northern Tian Shan, China. Tectonophysics 463, 60–68.
Sun, J.M., Zhang, L.Y., Deng, C.L., Zhu, R.X., 2008. Evidence for enhanced aridity in the Tarim Basin of China since 5.3 Ma. Quat. Sci. Rev. 27, 1012–1023.
Sun, J.M., Li, Y., Zhang, Z.Q., Fu, B.H., 2009a. Magneostratigraphic data on the Neogene growth folding in the foreland basin of the southern Tianshan Mountains. Geology 37, 1051–1054.
Sun, J.M., Zhang, Z.Q., Zhang, L.Y., 2009b. New evidence on the age of the Taklimakan Desert. Geology 37, 159–162.
Sun, J.M., Ye, J., Wu, W.Y., Ni, X.J., Bi, S.D., Zhang, Z.Q., Liu, W.M., Meng, J., 2010. Late Oligocene–Miocene mid-latitude aridification and wind patterns in the Asian interior. Geology 38, 515–518.
Sun, D.H., Bloemendal, J., Yi, Z.Y., Zhu, Y.H., Wang, X., Zhang, Y.B., Li, Z.J., Wang, F., Han, F., Zhang, Y., 2011. Palaeomagnetic and palaeoenvironmental study of two parallel sections of late Cenozoic strata in the central Taklimakan Desert: implications for the desertification of the Tarim Basin. Palaeogeogr. Palaeoclimatol. Palaeoecol. 300, 1–10.
Suppe, J., Chou, G.T., Hook, S.C., 1992. Rates of folding and faulting determined from growth strata. In: McClay, K.R. (Ed.), Thrust Tectonics. Chapman & Hall, Suffolk, pp. 105–121.
Suppe, J., Sabàt, F., Muñoz, J.A., Poblet, J., Roca, E., Vergés, J., 1997. Bed-by-bed fold growth by kink-band migration: Sant Llorenç de Morunys, eastern Pyrenees. J. Struct. Geol. 19, 443–461.
Tada, R., Zheng, H.B., Isozaki, Y., Hasegawa, H., Sun, Y.B., Yang, W.G., Wang, K., Toyoda, S., 2010. Desertification and dust emission history of the Tarim Basin and its relation to the uplift of northern Tibet. Geol. Soc. London Spec. Publ. 342, 45–65.
Tang, Z.H., Ding, Z.L., White, P.D., Dong, X.X., Ji, J.L., Jiang, H.C., Luo, P., Wang, X., 2011. Late Cenozoic central Asian drying inferred from a palynological record from the northern Tian Shan. Earth Planet. Sci. Lett. 302, 439–447.
Tang, Z.H., Huang, B.C., Dong, X.X., Ji, J.L., Ding, Z.L., 2012. Anisotropy of magnetic susceptibility (AMS) record of the Jingou River section: implications for late Cenozoic uplift of the Tian Shan. Geophys. Geochem. Geosyst. 13. http://dx.doi.org/10.1029/2011GC003966.
Tapponnier, P., Xu, Z.Q., Roger, F., Meyer, B., Arnaud, N., Wittlinger, G., Yang, J., 2001. Oblique stepwise rise and growth of the Tibet Plateau. Science 294, 1671–1677.
Trumbore, S.E., Chadwick, O.A., Amundson, R., 1996. Rapid exchange between soil carbon and atmospheric carbon dioxide driven by temperature change. Science 272, 393–396.
Vergés, J., Marzo, M., Muñoz, J.A., 2002. Growth strata in foreland settings. Sediment. Geol. 146, 1–9.
Walker, T.R., 1967. Formation of red beds in modern and ancient deserts. Geol. Soc. Am. Bull. 78, 353–368.
Wang, X., Sun, D.H., Chen, F.H., Wang, F., Li, B.F., Popov, S.V., Wu, S., Zhang, Y.B., Li, Z.J., 2014. Cenozoic paleo-environmental evolution of the Pamir–Tien Shan convergence zone. J. Asian Earth Sci. 80, 84–100.
Warny, S.A., Bart, P.J., Suc, J.-P., 2003. Timing and progression of climatic, tectonic and glacioeustatic influences on the Messinian Salinity Crisis. Palaeogeogr. Palaeoclimatol. Palaeoecol. 202, 59–66.
Wasson, R.J., Smith, G.I., Agrawal, D.P., 1984. Late Quaternary sediments, minerals, and inferred geochemical history of Didwana lake, Thar Desert, India. Palaeogeogr. Palaeoclimatol. Palaeoecol. 46, 345–372.
Windley, B.F., Allen, M.B., Zhang, C., Zhao, Z.Y., Wang, G.R., 1990. Paleozoic accretion and Cenozoic re-deformation of the Chinese Tien Shan Range, Central Asia. Geology 18, 128–131.
Xiao, G.Q., Abels, H.A., Yao, Z., Dupont-Nivet, G., Hilgen, F.J., 2010. Asian aridification linked to the first step of the Eocene–Oligocene climate Transition (EOT) inobliquity-dominated terrestrial records (Xining Basin, China). Clim. Past 6, 501–513.
Yang, S.L., Ding, Z.L., 2003. Color reflectance of Chinese loess and its implications for climate gradient changes during the last two glacial–interglacial cycles. Geophys. Res. Lett. 30, 2058. http://dx.doi.org/10.1029/2003GL018346.
Yin, A., Nie, S., Craig, P., Harrison, T.M., Ryerson, F.J., Qian, X., Yang, G., 1998. Late Cenozoic Tectonic evolution of the southern Chinese Tian Shan. Tectonics 17, 1–27.
Zachos, J., Pagani, M., Sloan, L., Thomas, E., Billups, K., 2001. Trends, rhythms, and aberrations in global climate 65 Ma to present. Science 292, 686–693.
Zhang, Z.Q., Sun, J.M., 2011. Palynological evidence for Neogene environmental change in the foreland basin of the southern Tianshan range, northwestern China. Global Planet. Chang. 75, 56–66.
Zhang, Z.S., Wang, H., Guo, Z., Jiang, D., 2007. What triggers the transition of palaeoenvironmental patterns in China, the Tibetan Plateau uplift or the Paratethys Sea retreat? Palaeogeogr. Palaeoclimatol. Palaeoecol. 245, 317–331.
Zhang, W.G., Yu, L.Z., Lu, M., Zheng, X.M., Ji, J.F., Zhou, L.M., Wang, X.Y., 2009. East Asian summer monsoon intensity inferred from iron oxide mineralogy in the Xiashu Loess in southern China. Quat. Sci. Rev. 28, 345–353.
Zheng, H.B., Chen, H.Z., Cao, J.J., 2002. Paleoenvironmental significance of the Pliocene–early Pleistocene eolian loess in the southern Tarim Basin. Chin. Sci. Bull. 47, 226–230.
Zheng, H.B., Powell, C., Butcher, K., Cao, J.J., 2003. Late Neogene aeolian loess deposition in southern Tarim Basin and its palaeoenvironmental significance. Tectonophysics 375, 49–59.
Zheng, D., Zhang, P., Wan, J., Yuan, D., Li, C., Yin, G., Zhang, G., Wang, Z., Min, W., Chen, J., 2006. Rapid exhumation at ~8 Ma on the Liupan Shan thrust fault from apatite fission-track thermochronology: implications for growth of the northeastern Tibetan Plateau margin. Earth Planet. Sci. Lett. 248, 198–208.
Zheng, D., Clark, M.K., Zhang, P., Zheng, W.J., Farley, K.A., 2010a. Erosion, fault initiation and topographic growth of the North Qilian Shan (northern Tibetan Plateau). Geosphere 6, 937–941.
Zheng, H.B., Tada, R., Jia, J.T., Lawrence, C., Wang, K., 2010b. Cenozoic sediments in the southern Tarim Basin: implications for the uplift of northern Tibet and evolution of the Taklimakan Desert. Geol. Soc. London Spec. Publ. 342, 67–78.
Zhu, Z.D., Wu, Z., Liu, S., Di, X.M., 1980. An Outline on Chinese Deserts. Science Press, Beijing.